PCCP

Physical Chemistry Chemical Physics

www.rsc.org/pccp

Volume 10 | Number 20 | 28 May 2008 | Pages 2869–3016

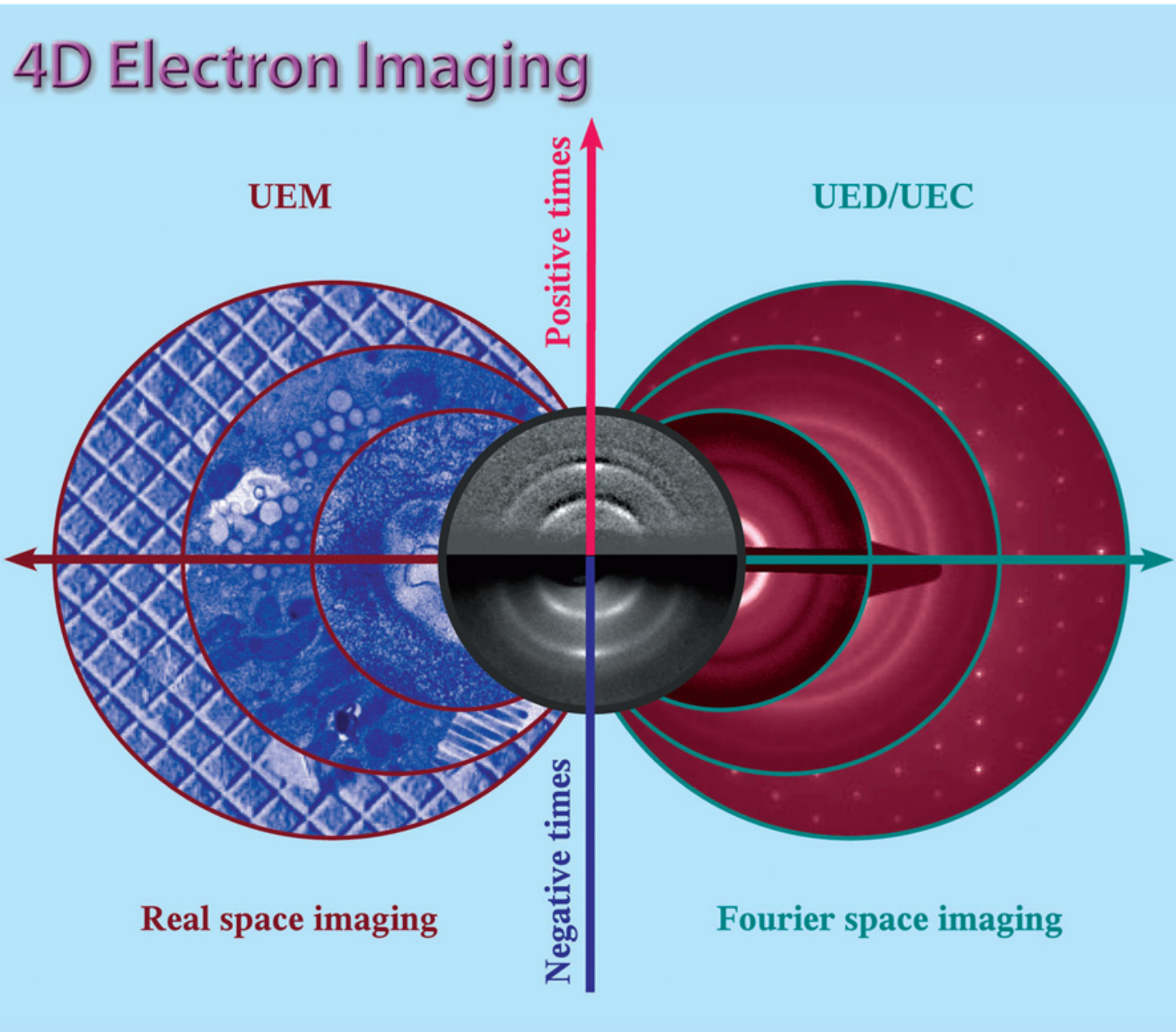

ISSN 1463-9076

COVER ARTICLE
Zewail and Shorokhov
4D electron imaging: principles and perspectives

ARTICLE
Zewail *et al.*
Ultrashort electron pulses for diffraction, crystallography and microscopy: theoretical and experimental resolutions

1463-9076(2008)10:20;1-4

4D electron imaging: principles and perspectives

Dmitry Shorokhov and Ahmed H. Zewail*

Received 29th January 2008, Accepted 3rd March 2008
First published as an Advance Article on the web 1st April 2008
DOI: 10.1039/b801626g

In this perspective we highlight developments and concepts in the field of 4D electron imaging. With spatial and temporal resolutions reaching the picometer and femtosecond, respectively, the field is now embracing ultrafast electron diffraction, crystallography and microscopy. Here, we overview the principles involved in the direct visualization of structural dynamics with applications in chemistry, materials science and biology. The examples include the studies of complex isolated chemical reactions, phase transitions and cellular structures. We conclude with an outlook on the potential of the approach and with some questions that may define new frontiers of research.

1. Introduction

In the 1980s, the field of femtochemistry was developed to observe in real time the transformations of reactants into products during the course of chemical reactions.[1] For elementary reactions[2] it was possible, by transition-state probing, to follow reaction trajectories on the femtosecond time scale of the motion. Experimentally, because the wavelength of the probe (optical) beam exceeds the atomic separations, structural changes were inferred for complex systems. Electron imaging provides the means for structure determination and during the transformation. Over the past years in this laboratory, the development of 4D electron imaging[3] has evolved into a field of study, which is now embracing ultrafast electron diffraction (UED), crystallography (UEC), and microscopy (UEM), and opening the door for applications in chemistry, materials science, and biology.[4] With the added dimension of time, and with the ever-increasing spatial and temporal resolution (currently, pm and fs, respectively), our focus is on direct visualization of structural dynamics in the four dimensions of space and time. Methods based on X-ray absorption and diffraction are not the subject of this perspective.[5] Here, we glimpse into history, outline key concepts, and give an overview which constitutes the basis of UED, UEC, and UEM, with examples for applications in the study of complex isolated chemical reactions and interfaces, phase transitions of materials, and macromolecular and cellular structures.

Studies with electrons have their origin in J. J. Thomson's 1897 discovery of the corpuscle and L. de Broglie's postulate of the electron's wave nature in 1924. As particles with pm wavelength, electrons can diffract with atomic-scale resolution and they can be focused in a microscope. The power of electron diffraction and electron microscopy is manifested in the myriad of applications in different phases: molecular structure determination of gases by L. Pauling and others (thousands of structures), structural characterization of surfaces and materials by low-energy electron diffraction (LEED) and reflection high-energy electron diffraction (RHEED), and determination of 3D macromolecular structures (including membrane proteins). Though electron diffraction by thin liquid films was first explored by L. R. Maxwell as early as 1933, it was not until 1974 that suitable diffraction patterns of liquid water were obtained.[6] Since electrons strongly interact with air, electron scattering measurements are usually performed in vacuum, unless environmental techniques, including cryomicroscopy in amorphous ice, are introduced. It is because of this strong interaction with matter that ultrashort electron pulses are capable of revealing transient structures of gases, surfaces, and (thin) crystals.

Physical Biology Center for Ultrafast Science and Technology, Arthur Amos Noyes Laboratory for Chemical Physics, California Institute of Technology, Pasadena, CA 91125, USA. E-mail: zewail@caltech.edu; Fax: +1 (626) 792 8456

Dmitry Shorokhov received his BS and MS from the Moscow Institute of Physics and Technology, and his PhD from the University of Oslo. Upon the award of Alexander von Humboldt postdoctoral fellowship, he moved to the Technical University of Munich and, subsequently, to the University of Augsburg. Following a postdoctoral stint with Prof. Zewail, he was appointed a senior scientist at Caltech.

Ahmed Zewail received the 1999 Nobel Prize in Chemistry, among other honors including postal stamps for his contribution to science and humanity. He is the Linus Pauling Chair Professor of Chemistry and Professor of Physics, and Director of the Physical Biology Center at Caltech. Current research focuses on 4D visualization and understanding of (macro)-molecular complexity.

2. Basic principles of 4D imaging

As with stop-motion photography and flash stroboscopy, in 4D imaging the molecular motion has to be resolved into frames using a sequence of flashes, in our case the probing electron pulses. (An educational exhibit that highlights the principle, and that is now on display at the Nobel Museum in Stockholm, has been described in detail elsewhere.)[7] However, 4D electron imaging demands the marriage of ultrafast probing techniques with those of conventional microscopy and diffraction, as well as the development of concepts describing the simultaneous temporal and spatial resolutions of atomic scale. Of relevance here is the "*uncertainty relationship*" between time and energy and the apparent "uncertainty" that may limit the spatial resolution.[8,9] Since the first reports from this laboratory, the technical and theoretical machinery had to be further developed, and currently at Caltech there are five table-top instruments for studies of gases, condensed matter and biological systems.[3] Examples of the experimental setups for UED, UEC and UEM are displayed in Fig. 1.

The conceptual framework of the approach is as follows. Upon the initiation of the structural change by either heating of the sample, or through electronic excitation induced by ultrashort laser pulses, a series of electron pulses is used to probe the specimen with a well-defined time delay. An electron diffraction pattern or a microscopy image is then obtained. A series of images recorded at a number of delay times provides a direct insight into the temporal evolution of the structure. Isolated reactions are studied by using collisionless molecular beams (UED), while crystals and surfaces are examined either in the reflection or transmission mode (UEC). For microscopy, the electron beam typically penetrates a nm-scale sample (UEM); see Fig. 1.

The leap forward in diffraction studies came from the integration of new 2D digital processing with CCD cameras, the generation of ultrashort electron packets using the photoelectric effect but with fs laser pulses and high extraction fields, and the *in situ* pulse sequencing and clocking—all of which gave unprecedented levels of sensitivity and spatiotemporal resolution to perform real experiments for determining structural dynamics, especially in molecular beams with no long-range order. One of the most critical advances was the development of the *frame-reference method*. When properly timed frame referencing is made, before and during the change, the evolving transient structures can be determined, as shown below.

For real-space imaging—microscopy—the strict requirement for proper focusing adds a real challenge. In order to reach the fs, and possibly the as range,[10] a new way of thinking was required. The paradigm shift was the realization that imaging can be achieved using timed and coherent single-electron packets,[3,11] which are free of space-charge effects. Images develop in about the same time as that of an *N*-electron pulse, but now the time resolution is under control. Increasing the number of electrons in the pulse can, in principle, result in a single-pulse imaging, especially suited for irreversible processes that result in permanent damage. There is another dimension to UEM, namely the *in situ* observation of nano-scale physical and mechanical phenomena and biological imaging with ultrashort electron pulses, as discussed below.

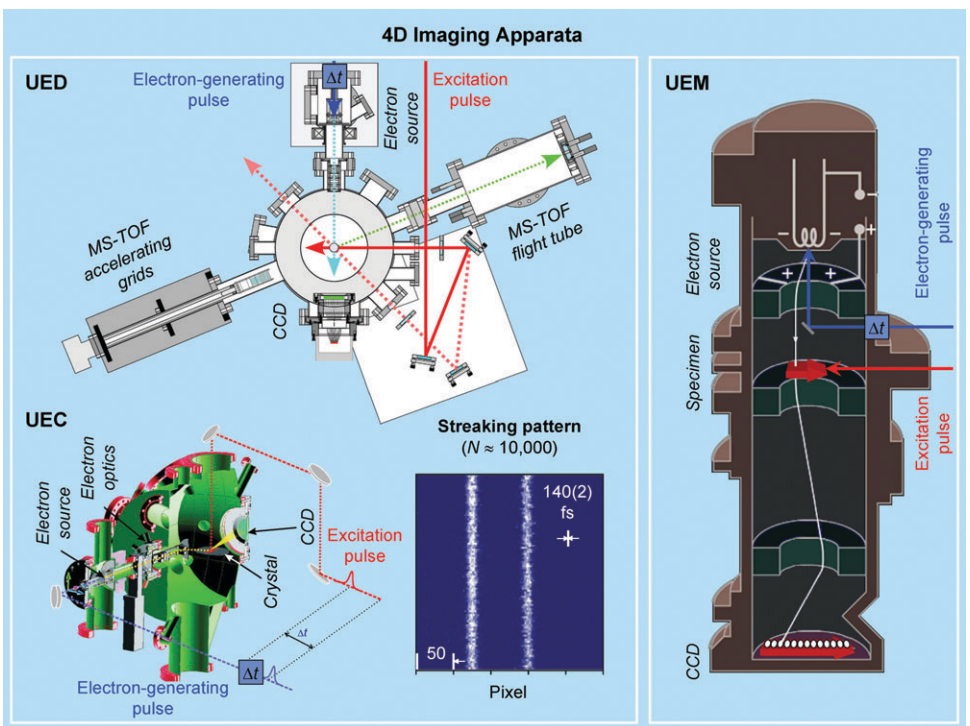

Fig. 1 4D imaging apparata for ultrafast electron diffraction (UED), crystallography (UEC) and microscopy (UEM). Note the single-electron trajectory schematized in UEM. Inset: Streaking pattern for pulses of about 10 000 electrons in UEC.

At 200 kV, the de Broglie wavelength of our newly-designed UEM microscope (Fig. 2)[12] is 2.5 pm. Unlike photons (bosons), electrons (fermions) can singly occupy a certain volume of space which defines the spatial resolution in imaging. Given the speed of electrons and their dispersion and the divergence angle, it was shown that single-electron imaging can be achieved coherently in a volume of $\sim 10^7$ nm^3, with atomic-scale resolution. This is an important point for studies of dynamics. Finally, a note regarding structural dynamics in crystals is appropriate here. The intensity I of a Bragg spot (hkl), which is proportional to the square of the structure factor

$$F(hkl) = \sum_j f_j \exp[-2\pi i(hkl) \cdot (xyz)_j], \qquad (1)$$

where f_j is the atomic scattering factor, is determined by the position (xyz) of the atom j within the unit cell. Thus, intensity changes of Bragg spots are associated with motions of atoms within the unit cell, and these changes can be determined by the structure factor monitored in the intensity of scattered electrons for a given direction and zone axis. Such selectivity permits the establishment of the pathway for structural change, as indicated below.

3. Applications

3.1 Chemical reactions

With a properly-chosen frame referencing, *i.e.*, with an adequate selection of the two points in time which correspond to the two different states of the system under study, typically before ($t < 0$) and after ($t > 0$) the arrival of the exciting laser pulse, the spatiotemporal evolution of transient structures has now been extensively explored for different chemical processes.[3] A classic example is the transient behavior observed upon consecutive elimination of iodine from 1,2-diiodotetrafluoroethane ($C_2F_4I_2$) to form tetrafluoroethylene (C_2F_4) on the ultrafast time scale,[13] and the determination of the structure of the ps-lived C_2F_4I intermediate (Fig. 3).

In order to resolve structural changes during the course of the elimination reaction, the diffraction pattern of the *anti–gauche* conformation mixture characteristic of the ground state of $C_2F_4I_2$ at $t = -95$ ps (Fig. 3) was referenced by those obtained for a variety of time points corresponding to $t > 0$, and the resulting *diffraction differences* were analyzed. The significance of this referencing is evident in the results of Fig. 4; a reference at positive time shows the absence of I··I nonbonded distance, as the first C–I bond breaks on the sub-ps time scale. The results of least-square structure refinements supported the nonconcerted nature of the reaction: the first step ($C_2F_4I_2 \rightarrow C_2F_4I + I$) is essentially complete within 5 ps (see evolution in Fig. 4), whereas the second step ($C_2F_4I \rightarrow C_2F_4 + I$) takes place with a time constant of 26 ± 7 ps. The structure of the intermediate was determined using the difference curves. The first step is dissociative and occurs in $\sim$200 fs.[14]

Knowing the time scales involved, two structures were considered for C_2F_4I: a *classical* structure, in which the primary halide (I) resides predominantly on one $-CF_2$ moiety, and a *bridged* structure, in which the primary halide is shared equally between the two $-CF_2$ moieties (Fig. 3). To explore

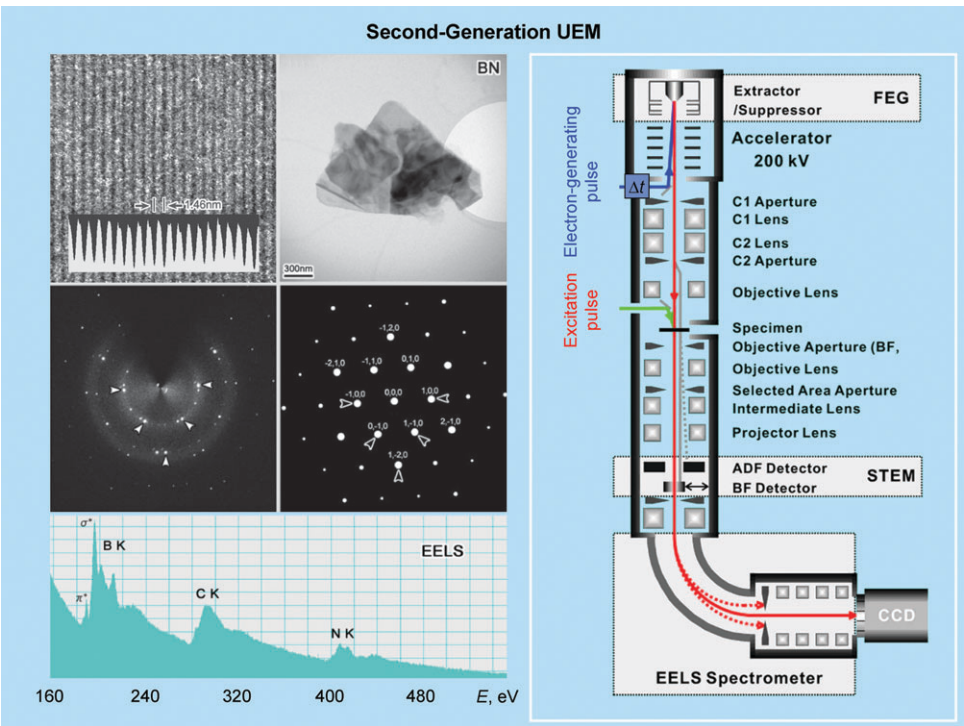

Fig. 2 Second-generation UEM apparatus (UEM-2) which is equipped with scanning and EELS capabilities (right). Microscopy images showing molecular planes in real space and boron image map, diffraction patterns (atomic resolution) and electron energy loss spectra (EELS), all taken with Caltech's 200 keV UEM (left).

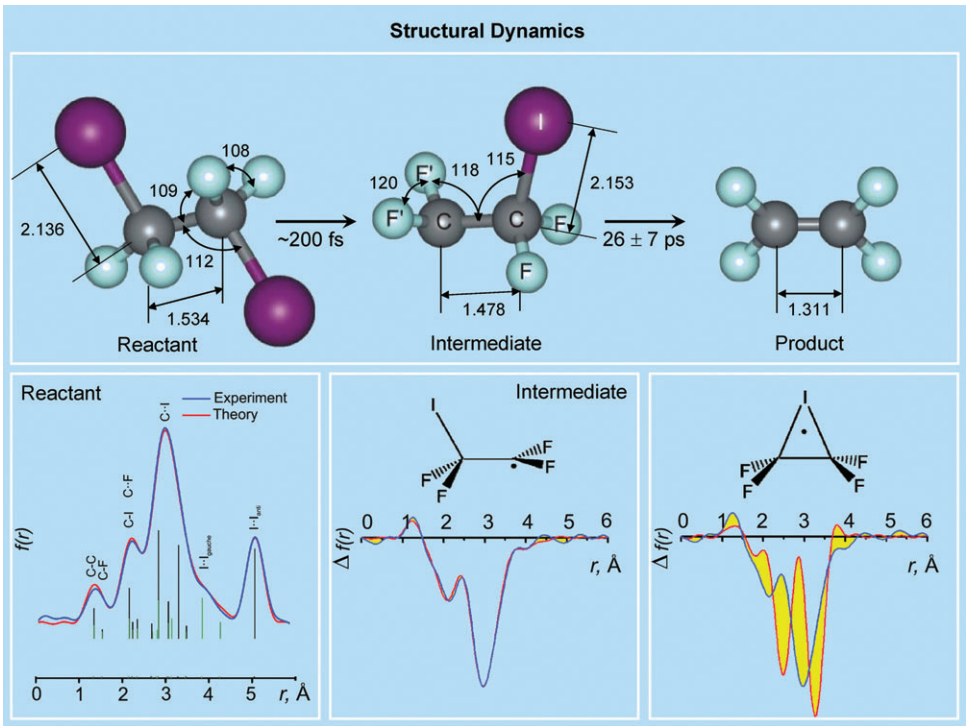

Fig. 3 Structural dynamics of the elimination reaction of $C_2F_4I_2$, with the reactant, intermediate and product structures determined under collisionless condition (top). UED patterns of the *anti–gauche* conformation mixture characteristic of the reactant as obtained for the ground state. Internuclear distances for the *anti* (black) and *gauche* (green) isomers are indicated by vertical bars at the bottom of the panel (lower left). The structure of the intermediate is determined to be classical (lower center), not bridged (lower right), as evidenced by the agreement between diffraction theory and experiment; the discrepancy between theory and experiment is indicated in yellow.

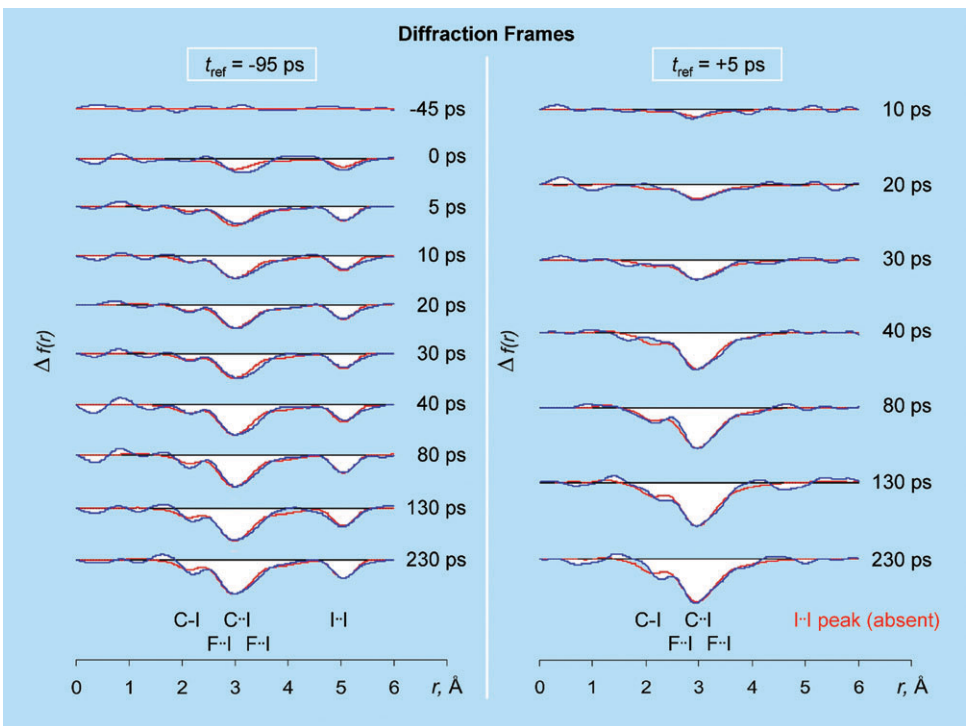

Fig. 4 Frame-referencing methodology applied to the determination of structures in the elimination reaction of $C_2F_4I_2$. Temporal changes in diffraction with respect to the two different reference points, before (left) and after (right) the arrival of the exciting laser pulse, are shown. Note the absence of the I··I peak in the right panel.

detailed structural features of the radical, the diffraction difference curves were averaged and fit separately with either the bridged radical structure or the classical *anti* and *gauche* radical structures obtained using *ab initio* calculations.[15] Theoretical curves for the classical structures provide an excellent fit to the experimental data, whereas the fit to the bridged structure is very poor (Fig. 3), thereby elucidating the nature of the intermediate: the structure of the C_2F_4I radical is classical.

The evolution of the reaction reflects changes in bond distances and angles. The C–I and C–C distances of the intermediate [2.153(13) and 1.48(5) Å] are, respectively, longer and shorter, than those of the reactant [2.136(7) and 1.534(13) Å]. These results elucidate the increased C–C and decreased C–I bond order resulting from the formation of the transient C_2F_4I structure. Moreover, the C–C–F′ and F′–C–F′ angles (Fig. 3) become larger than the corresponding angles of the reactant (by $\sim$9 and $\sim$12°, respectively), suggesting that the intermediate relaxes following the loss of the first I atom. The structures and dynamics reported for this reaction are vital in describing the retention of stereochemistry in this class of reactions, and this is the first example of resolving such complex structures during the transition to final products. One important conclusion is that the retention of stereochemistry is dynamical in origin (not electronic) in that the bonds break before rotation scrambles the orientation.

3.2 Molecular interfaces

The example discussed here for molecular assemblies is that of probing, using UEC, nm-scale layers of water on substrates, following an ultrafast laser-induced temperature jump. An insight into both the structure and dynamics of interfacial water layers on hydrophilic (silicon, chlorine-terminated; Fig. 5) and hydrophobic (silicon, hydrogen-terminated or silver-coated) surface substrates was recently obtained.[16] The time scales for energy transfer and disruption of the hydrogen-bond network were reported as well, elucidating the mechanism at the molecular level. Structurally, the nature of water on a substrate is determined by forces of orientation at the interface and by the net charge density, or *type*, of the substrate, whereas the transformation from ordered to disordered structures, and their coexistence, must depend on the time scales for the movements of atoms locally and at a long range.

On the hydrophilic surface substrate the structure is found to be cubic (I_c), not hexagonal (I_h), and on the hydrophobic surface, the structure although is still cubic, is very different in the degree of order. Though the interface is dominated by polycrystalline I_c, coexisting in this phase are crystallite structures, which are adjacent to the surface of the substrate. Interestingly, the time scale for losing the hydrogen bond network when hydrophilic substrate is used (37 ps, *cf.* 700 fs to 1.5 ps characteristic of bulk liquid water) is similar to that found for interfacial water near hydrophilic protein surfaces (20 to 50 ps).[17] We have also studied the same assembly on hydrophobic substrates and in section 3.4 we discuss the application of UEC to probe assemblies of bilayers on substrates and using the temperature jump to induce structural changes.

3.3 Phase transitions

Because of the combined microscopy–diffraction capabilities of UEC and UEM, they provide unique dimensions in study of phase transitions, quantum wells and novel materials of nm-length scale. Two examples are given here for studies of temperature-induced metal–insulator phase transitions in vanadium dioxide (VO_2) and of nonequilibrium structural transitions in superconducting cuprates. Metal–insulator phase transitions are abundant in many systems.[18]

UEM imaging of films of VO_2 reveals clearly the occurrence of the phase transition in crystallites of the nm scale (Fig. 6). Both the ultrafast insulator-to-metal transition and the slower recovery were observed, and theoretical considerations of the effects of connectivity and diffusion account for the observed behavior.[19,20] The UEC study was performed both on films and on single crystals of VO_2. The phase transition exhibits a well-defined hysteresis between the two thermodynamically-stable structures (Fig. 6). In order to map pathways of motion, all observed Bragg diffractions of different planes and zone axes were examined on the fs-to-ns time scale.[21] As with chemical reactions, discussed above, the concept of concerted (or concurrent) *vs.* consecutive nuclear motions, which deal with reorganization of the lattice and microscopic restructuring within unit cells, becomes important to understanding the elementary steps of the mechanism. Because the transformation takes place in a strongly correlated system, the dependence on excitation fluence is evident in a threshold behavior, and we studied such dependence at short and long times to elucidate the nonequilibrium transition from local atomic motions to shear at sound wave (and carrier) velocity.

The 3D sampling of diffraction and long-range order studied allow for the separation of different nuclear motions, which are mirrored in the temporal change of the structure factor for various Miller indices. For two different kinds of investigated Bragg spots (*hkl*), characterized by $h \neq 0$ and $h = 0$, two different types of dynamics were observed: a fs process (307 fs) and another process with a time constant 9.2 ps. This distinct behavior in dynamics indicates stepwise atomic motions along different directions. Because an atomic movement along a certain direction can only affect such Bragg spots that have nonzero contributions in the corresponding Miller indices (eqn (1)), it was concluded that the initial fs motion is along the *a*-axis (Fig. 6), which is the direction of the V–V bond in the monoclinic structure. From a chemical perspective, the excitation is to an antibonding state, which instantly results in a repulsive force on the atoms, and they separate along the bond direction. In sequence and on a slower time scale, the unit cell transforms toward the configuration of the rutile phase.[22] On the ns time scale, the system reaches equilibration nearly at sound wave shear motion. These observations of stepwise atomic motions indicate that the phase transition proceeds by a nondirect pathway on the multi-dimensional potential energy surface and not by a direct structural conversion, thus defining a transition-state intermediate for the metal-to-insulator transition.

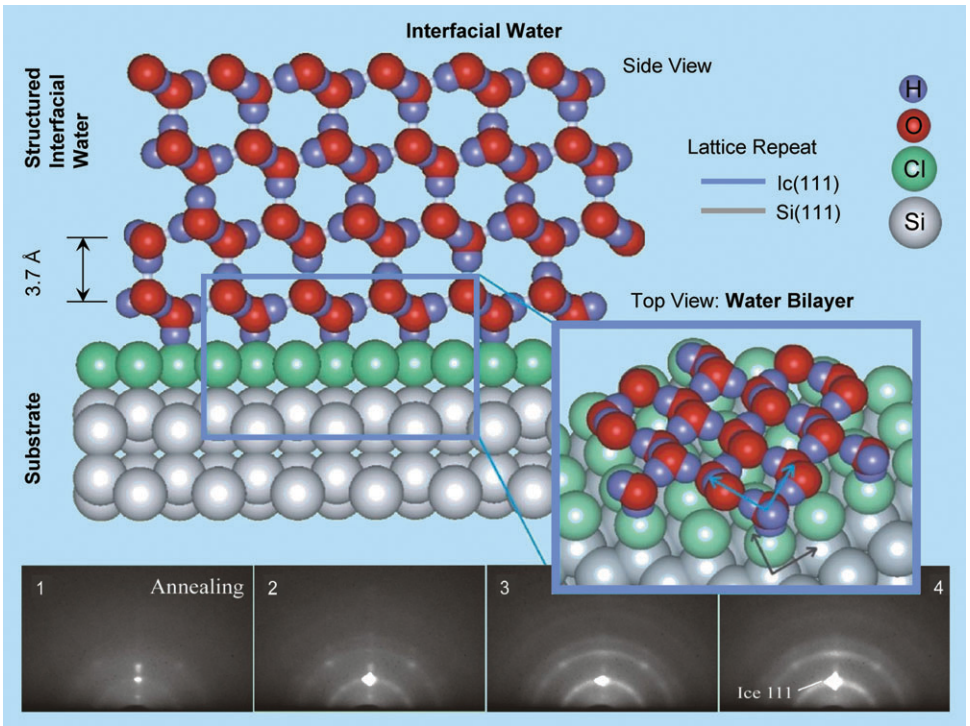

Fig. 5 Structural dynamics of interfacial water at the hydrophilic interface. The chlorine termination on a Si(111) substrate forms a hydrophilic layer that orients the water bilayer. The ordered stacking persists for three to four bilayers ($\sim$1 nm) before disorientation takes place and results in crystallite islands, forming the layered structure. Note the coexistence of two phases as evidenced by Bragg spots and Debye–Scherrer rings.

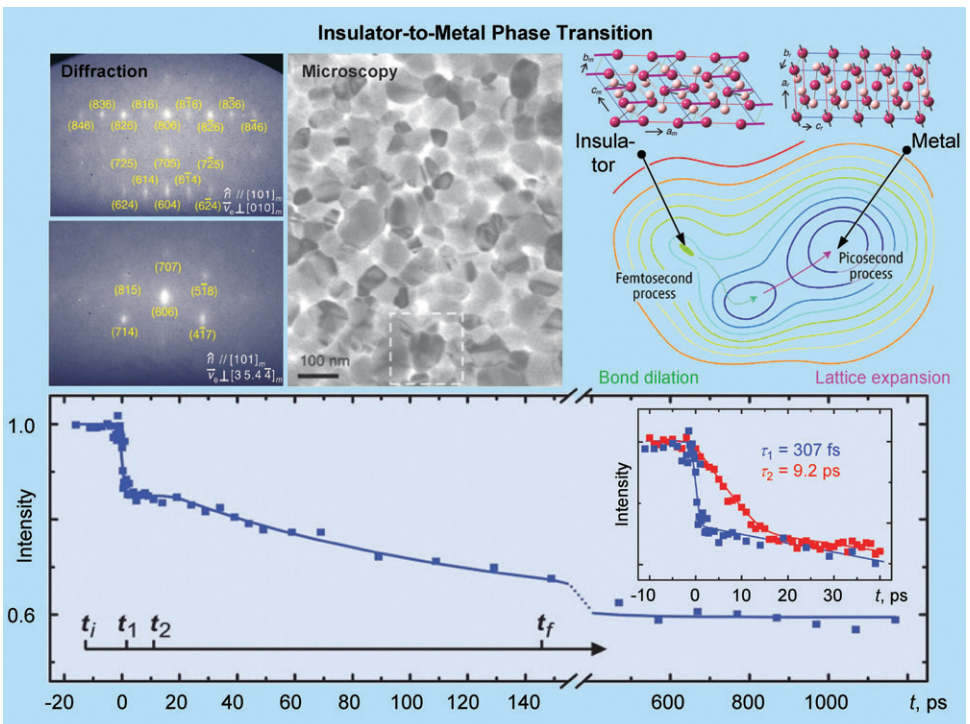

Fig. 6 Structural dynamics of the insulator-to-metal transition of vanadium dioxide. Bragg diffractions (upper left) of different directions (***n***) and zone axes ($\boldsymbol{v}_e$), when temporally resolved, indicate that the phase transition between the initial (monoclinic) and the final (tetragonal) structure (upper right) occurs stepwise in the order of fs and ps, as depicted in the two-coordinate energy landscape (center right). The full temporal behavior is illustrated at the bottom. Real-space (microscopy) image as obtained using UEM-1 is shown to indicate the nm scale of crystallites (upper center).

The second example for nonequilibrium structural phase transitions is that of superconducting cuprates.[23] The specific material studied is oxygen-doped $La_2CuO_{4+\delta}$ (LCO); the undoped material is an antiferromagnetic Mott insulator, whereas doping confers superconductivity below 32 K and metallic properties at room temperature. From the observed Bragg spots, the following unit-cell parameters were obtained using the patterns for different zone axes: $a = b = 3.8(1)$, $c = 13.1(1)$ Å.[24] Structural dynamics were then obtained by recording the diffraction frames at different times, before and after the arrival of the optical excitation pulse. What was expected, as observed in previous UEC studies in this laboratory, is that the peak shifts continuously and the intensity decreases with time. Instead, all curves obtained at different times cross at a single value of *s*-coordinate which parametrizes the momentum-transfer space. This intensity sharing with a common crossing point, a structural *isosbestic point*, indicates a transition from the initial phase to a new (transient) phase.

The structural interconversion displaying the isosbestic point is illustrated in Fig. 7. The diffraction difference profile, as a function of time, reveals the depletion of initial structure and the accumulation of the transient-phase structure. The population of the initial (transient) phase decays (builds up) with a time constant of 27 ps, but the formed phase restructures on a much longer time scale (307 ps). Because the linear expansion coefficient is $\alpha_l \leq 1.0 \times 10^{-5}$ K^{-1}, the observed 2.5% increase in the lattice constant would correspond to an unphysical 2500 K rise in the lattice temperature at equilibrium. Another striking feature of this structural phase transition is its dependence on the fluence of the initiating pulse. A threshold was observed, above which the lattice constant of the transient-phase structure changes linearly with the fluence (Fig. 7).

The transformation at 1.55 eV is the result of a charge transfer from oxygen (O^{2-}) to copper (Cu^{2+}) in the *a*–*b* copper–oxygen planes, as reported in the literature. With the lattice relaxation being involved, the excitation is shared microscopically (exciton type), and finally a transition to a transient phase is made (macroscopic domain). The net charge distribution in the transient phase results in the weakening of interplanar Coulomb attractions, leading to expansion along the *c*-axis. The behavior is nonlinear in that when the number of transformed sites is below a critical value, the macroscopic transition is not sustainable. The crystal domain is greater than 20 nm^2 and symmetry breaking is not evident because charge transfer is in a plane perpendicular to the *c*-axis expansion. By consideration of Madelung energy and charge distributions, the linear dependence on fluence and the large values of expansion were accounted for.

The transient-phase structures, which are inaccessible by means of equilibrium methods, are undetectable by optical probes with wavelengths longer than lattice spacings. Moreover, the time scales of optical response and structural changes are very different. For the cuprate studied, the observed phase transition is the result of electronic charge redistribution and lattice collective interactions to form domains. The similarity of the apparent threshold for "photon doping" at ~0.12 photons per copper site and the "chemical doping" at fractional charge of 0.16 per copper site, required for

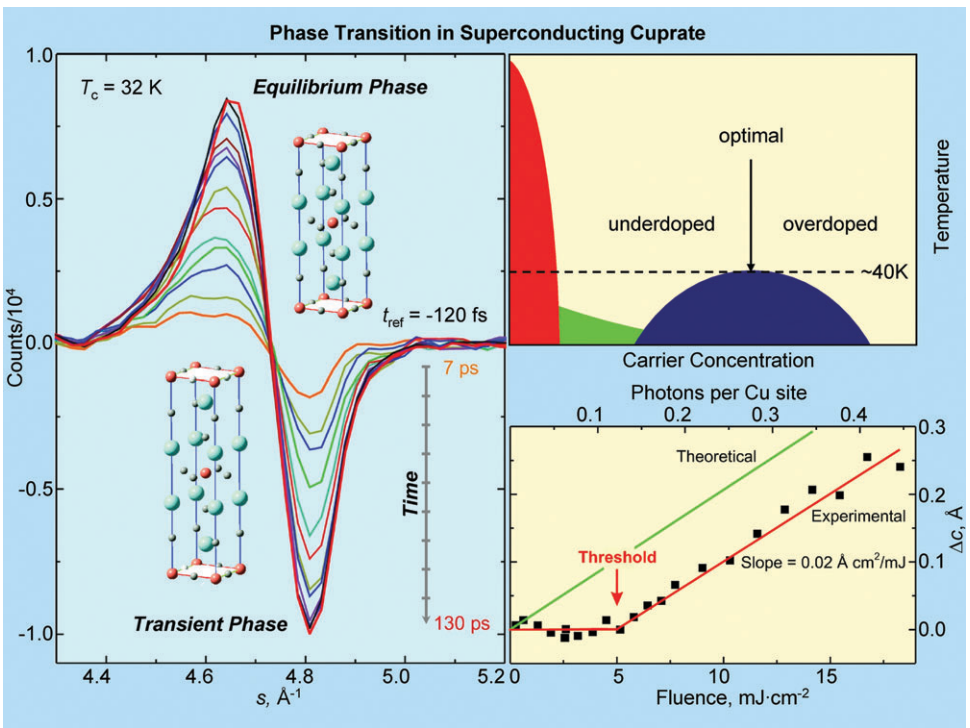

Fig. 7 Structural phase transition in oxygen-doped cuprate, $La_2CuO_{4+\delta}$, and its schematic phase diagram (upper right). The temporal evolution of the diffraction difference profile indicates the depletion of the initial structure and the build up of the transient-phase structure (left). Lattice constant change as a function of fluence of the initiating pulse is shown at lower right. Note the presence of the isosbestic point at ~4.76 $Å^{-1}$ and the threshold at ~5 mJ cm^{-2}, which corresponds to a critical value for the number of photons per copper site (see text).

superconductivity, may have its origin in the nature of the photoinduced inverse Mott transition. If general, the implications are significant. More recently, we have extended these studies to graphite,[25] and in this case the formation of graphene due to structural distortions was the prime focus.

3.4. Biological structures

It has long been known that quasi-periodicity of assembled molecular layers, as opposed to the random orientations in the bulk, is a key factor of membrane functionality. Because of their resemblance to naturally-occurring biological membranes, Langmuir–Blodgett films often serve as models for studying membrane structures and properties. Perhaps the simplest representative of membrane-type structures is a layered deposition of aliphatic chain molecules on a hydrophilic or hydrophobic substrate. Experimentally, UEC is well suited to study the films because of its high sensitivity and low damage at low electron flux. Recently, we studied the structural dynamics of monolayer, bilayer and miltilayer adsorbates of crystalline fatty acids and phospholipids on silicon, hydrogen-terminated (hydrophobic) and oxide-terminated (hydrophilic) substrates.[26] In these studies, spatially-aligned aliphatic chains were immobilized in parallel layers on the substrates, and the structural change was initiated by fs near-infrared laser pulses. The combined unit-cell structures and dynamics following the temperature jump in the substrates provide insights into the nature of atomic motions and energy transfer from the substrate to the (multi)layered membrane-like adsorbates.

From these studies of the nonequilibrium structural dynamics of fatty acids (Fig. 8) and phospholipids,[27] the following picture has emerged. Because the aliphatic chains have no resonance absorption at the wavelength of the heating laser pulses, the energy is absorbed exclusively by the substrate. Within a few ps, the energy is transferred into the substrate lattice motions, which results in an expansion of the lattice. On this time scale, the energy flows along the aliphatic chains through vibrational motions. The net effect is elongation of the CH_2–CH_2–CH_2 subunits, which is determined by the impulsive force (or local temperature) of the substrate. Unlike the thermally-equilibrated expansion given solely by the thermal expansion coefficient, the nonequilibrium expansion depends on the actual distribution of excitation energy in the chains and, consequently, on the chain length and overall film thickness. In the UEC experiments, both the observed net amplitude for the change and its temporal evolution were found to be that of a nonequilibrium wave-type disturbance propagation at ultrashort times and subsequent thermal equilibration at much longer times. The key observation made was the extension of the CH_2–CH_2–CH_2 subunits by a significantly large percentage, when compared with the thermal value, indicating a coherent (ballistic) buildup of amplitudes at near the speed of sound propagation.

The transport of heat at early times induces a transient disorder, which causes the intensity of the pertinent diffraction feature to decrease during the first 15 ps. This result is expected in a Debye–Waller picture, as the degree of inhomogenity along the chains increases with temperature. However, with time, the adsorbate enters a more ordered state, which manifests itself in an increased diffraction intensity even above the

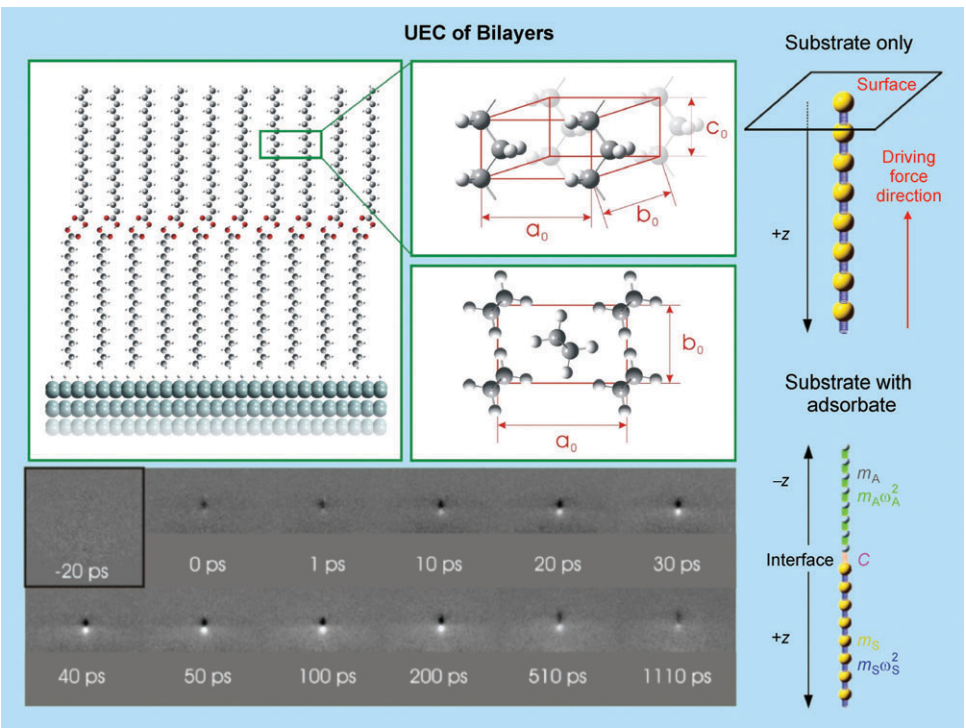

Fig. 8 Ultrafast electron crystallography of 2D fatty-acid bilayers (upper left). Shown are the subunit cell structure determined (upper center) and the dynamics obtained by frame referencing, following the heat pulse transfer to the substrate (lower left). The frames at 0 and 1 ps show the onset of structural changes, and the frames at longer times display the restructuring toward the equilibrium state. Also shown are the 1D atomic chains which represent substrate-only (upper right) and substrate–adsorbate (lower right) lattices used in our theoretical model.

initial value. This effect reflects the presence of an energy barrier, and that through alignment of the aliphatic chains by rotation and other motions, and possibly through transient annealing of the film, the ordered phase is dynamically possible. The enhanced structural ordering may be common, even in self-assembly, but it can only be observed in the non-equilibrium state at short times. It may also be significant to dynamic assembly and collective motions (which occur at short times) in bilayers and possibly membranes. A comprehensive theoretical account of the energy redistribution in both substrate and adsorbate at pertinent time scales has been reported,[28] and future work will consider the role of hydration. Self-assembled systems exhibit more diffuse scattering, but at shorter times some order was revealed.[29]

For biological cell structures, the angstrom-scale spatial resolution characteristic of its state-of-the-art apparatus renders electron microscopy arguably the most powerful tool for imaging. Our UEM, besides its dynamics capability, has the potential for providing higher image resolution and (possibly) less damage. As the first step towards implementation of the new technique, a cell of a baby-rat intestine was imaged using our first-generation electron microscope (UEM-1) operating in UEM (Fig. 9)[30] and TEM modes. Though it still remains to be seen to which extent UEM is less destructive as compared to TEM (notably, the overall electron dosage received by the sample should be pretty much the same in both cases), biological UEM promises unique applications, given the temporal resolution and spatial sensitivity achieved.

3.5 Mechanical and melting phenomena

As mentioned above, there is another dimension to UEM, namely the study of *in situ* structural transformations and melting which may occur on long time scales. A recent study of such transitions in quasi-1D semiconductor copper-7,7,8,8-tetracyanoquinodimethane (Cu-TCNQ), carried out using UEM-1, led to the discovery of a mechanical nanoscale molecular phenomenon, a switchable channel or *gate* (Fig. 10).[31] The control of the gate was made using the excitation shock induced in the sample by near infrared laser pulses. Remarkably, the switching, after a shock, is not only reversible with the pulses being on or off, but also returns the material in space to the original structure. The functional behavior is robust in the relatively low-fluence regime. At significantly higher fluences, we observed, in the microscope, the internal dilation and the reduction of the copper ions to form islands of neutral copper metal structures.

The mechanism as obtained from the microscopic diffraction patterns and macroscopic images involves a nonthermal electron transfer processes. In single crystals of Cu-TCNQ charge-transfer complex, Cu^+ and $TCNQ^-$ form discrete columnar stacks in a face-to-face configuration with strong overlap in the π-system. Further, the copper atoms are bound in a four-coordinate highly distorted tetrahedral geometry to the nitrogen atoms on the cyano groups of the TCNQ. The strong through-space interactions between the π-electrons result in the quasi-1D structure of the material in the solid state. As seen in the crystal structure in Fig. 10, the *a*-axis is unique for stacking. The large anisotropy of gating reflects the unique changes along the stacking axis [100] and not perpendicular to it. The modulation (*i.e.*, closing and opening) of the channel is a modulation of the π-electron interactions of the stacked TCNQ molecules as a result of the charge transfer from $TCNQ^-$ to Cu^+. This same reduction process is responsible for the formation of metallic copper islands at higher fluences.

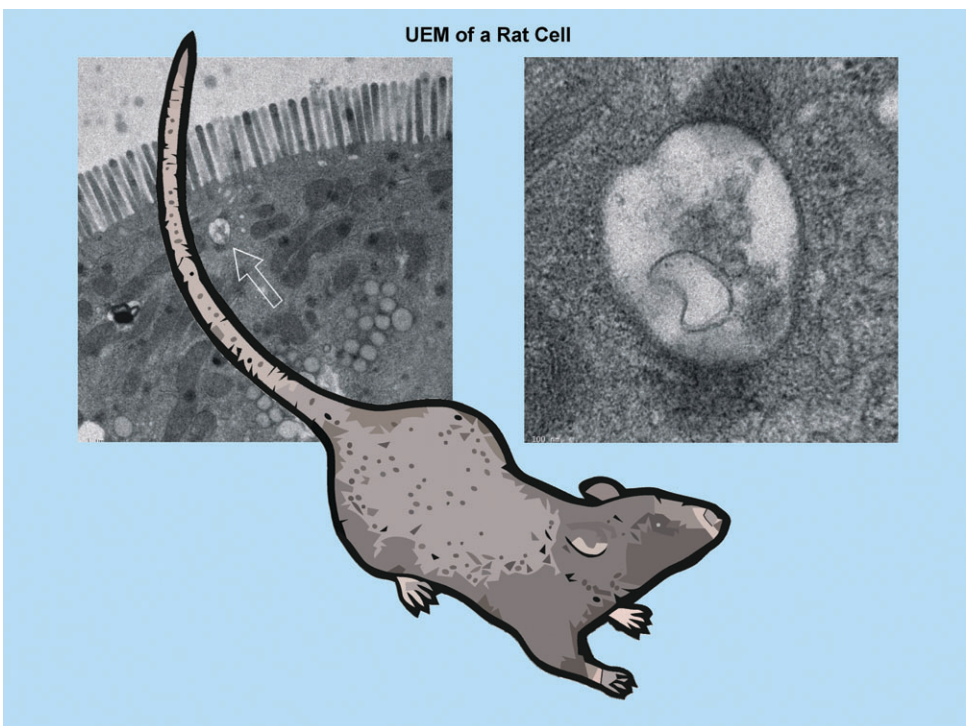

Fig. 9 UEM images of positively stained rat intestinal cells. The images show the microvilli in the intestinal epithelium of the neonatal rat along with numerous small vesicles throughout the cytoplasm. The arrow on the left indicates the vesicle magnified on the right.

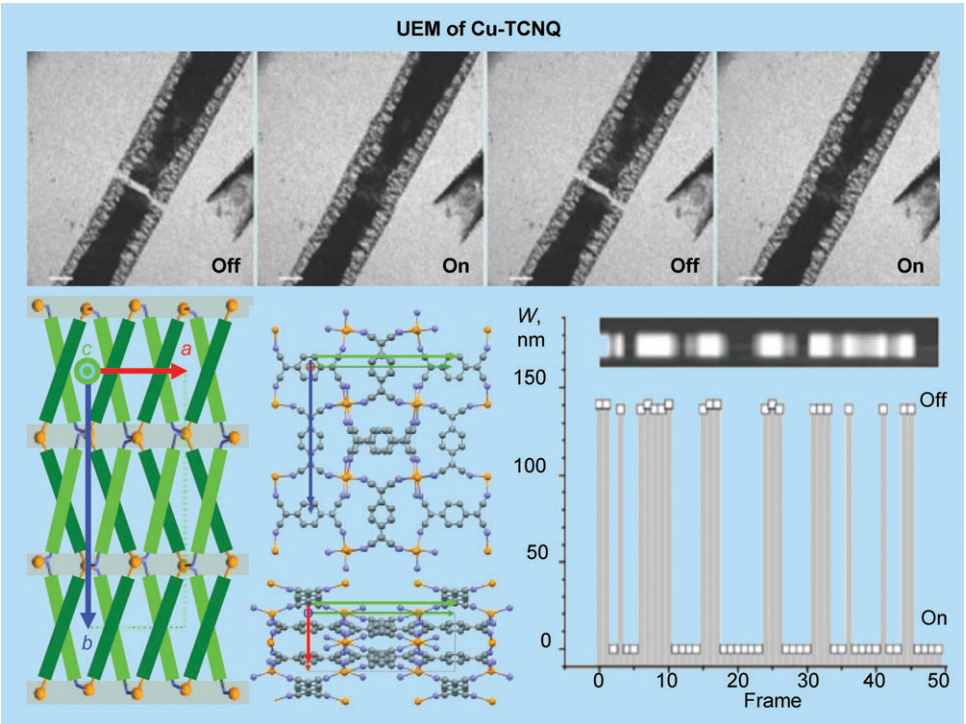

Fig. 10 UEM images of channel gating in the already shocked single crystal of Cu-TCNQ in the absence (''off'') and in the presence (''on'') of pulsed-laser irradiation (top), and a plot showing the results of a sequence of ''on'' and ''off'' cycles. The channel width W varied from 0 (pulsed-laser irradiation) to 140 $\pm$ 5 nm (no pulsed-laser irradiation) over a series of 50 frames. The bar in the inset is to illustrate the modulation in a memory recording (lower right). Crystal structure of Cu-TCNQ is shown in the lower left panel.

4. Theoretical

Central to the approaches discussed here is the generation and propagation of ultrafast coherent electron packets in space and time. Although the spatial resolution can reach the atomic scale, imaging must take into consideration the coherence volume of a single electron and the nature of the contrast function in the pulsed mode. The temporal resolution is typically limited by the probing-pulse width and by the difference in group velocities of electrons and the light used to initiate the dynamical change. With ''tilted'' optical pulses we can now reach limits of time resolution down to regimes of fs and, possibly, as.[10,21,32] The ever-ongoing theoretical research in the areas of laser and electron optics is expected to provide a solid ground for further experimental developments in our laboratory.

Due to the complex nature of the transitional phenomena under study, experiment and theory often have to go hand in hand in unraveling details of the microscopic forces involved. For structural determination, the initial ''*guess*'' structure is usually obtained from theory. In the UED of isotropic gases, a 3D molecular structure is projected onto a 1D momentum transfer space as a superposition of damped oscillations, each of which represents a particular internuclear separation r_{ij}. A molecular model based on some estimated structure parameters and vibrational correction terms has to be constructed and further refined using a least-squares fitting procedure until a reasonable agreement between the experimental and calculated scattering intensities is achieved. Both molecular structure parameters and vibrational corrections are typically obtained from quantum chemical calculations. A Fourier transform can then be used to obtain a *radial distribution function*, $f(r)$, which provides a snapshot of the density distribution of internuclear distances throughout the molecule at a particular point in time.[33] However, it is always important to examine parent scattering intensities for self-consistency. Based on developments in genetic algorithm techniques for structure solution from powder-diffraction data,[34] it was recently demonstrated that molecular structures and conformations can be determined from UED using a genetic algorithm.[35]

Of special interest to us is the study of biological structural changes free of the effects of solvent. Theory is a guiding force when considering the myriad of structural configurations and the unique features of diffraction. The UED methodology suffices to observe helix-to-coil structural transitions in proteins, which in solution occur on the ns time scale. However, for a protein, the problem is nontrivial as the detailed information regarding individual bond distances, valence angles, and conformations may not be readily available from the electron-scattering data. For example, in order to investigate the unfolding of a helix-rich protein upon a rapid temperature jump, we must take into account all possible final conformations. This complexity may, naively, suggest the masking of any significant change in diffraction. However, an accurate theoretical mapping of helix-to-coil transitions in a large molecular ensemble indicates that the problem of tracking down the disruption of the helical ordering in space and time is tractable. Due to the unique ''*spatial resonance*'' associated with the secondary structure in the protein, the ensemble-

averaged radial distribution function, $\langle f(r) \rangle$, provides an experimental criterion with which to evaluate the residual helicity in a molecular ensemble at each particular point in time (Fig. 11).[36]

Vectorial properties associated with molecular structure and rotational dynamics add a new dimension to UED, arising through the imposition of spatial order on otherwise randomly oriented ensembles (Fig. 11). In a recent series of publications,[37] which generalized the previous results,[38] the anisotropic scattering was found to be distinct from that of isotropic patterns. We reexamined their time-dependent manifestations in UED, and worked out a theoretical treatment to include arbitrary polarization directions and laser-induced sample distributions. To achieve this result, the molecular scattering intensity was given as an expansion in terms of the moments of the transition-dipole distribution created by the linearly-polarized excitation laser pulse. The isotropic scalar contribution thus obtained depends only on population dynamics and scalar internuclear separations, whereas higher moments reflect bond angles and evolve in time due to rotational motion of the molecules. By an analytic separation of the angular and isotropic signals, the properties of both information subsets are made accessible to analysis.[37]

Compared to thermally-equilibrated molecular ensembles characterized by Boltzmann probability density distributions, nonequilibrium molecular ensembles represent a real challenge to both experiment and theory. The non-Boltzmann molecular ensembles are typically dominated by far-from-equilibrium structures accumulating in the vicinity of classical turning points of a potential well. Depending on the energy of the pumping radiation, the ensemble-averaged structures may either approach the equilibrium structure, or may significantly deviate from it. Because the overall probability density distribution across the ensemble is given by a population-weighted average of probability densities characteristic of individual states of the system, ensemble-averaged deviations from equilibrium structures may strongly depend on the actual monochromaticity profile, δE, of the exciting radiation. In a recent review we outlined, for a δE of a Gaussian distribution function, how non-Boltzmann probability-density distributions can be calculated for strongly-anharmonic vibrations in homonuclear diatomics, and how the resulting nonequilibrium features manifest themselves in UED patterns.[33] Similar equations can also be solved for an arbitrary bonding potential and for a rotational Hamiltonian characterized by a number of intramolecular torsions. In this regard, Monte Carlo methods have been invoked to determine conformational dynamics for large systems.[39]

For crystals and interfaces, it is important to identify the nature of microscopic forces. Theoretical models are significant

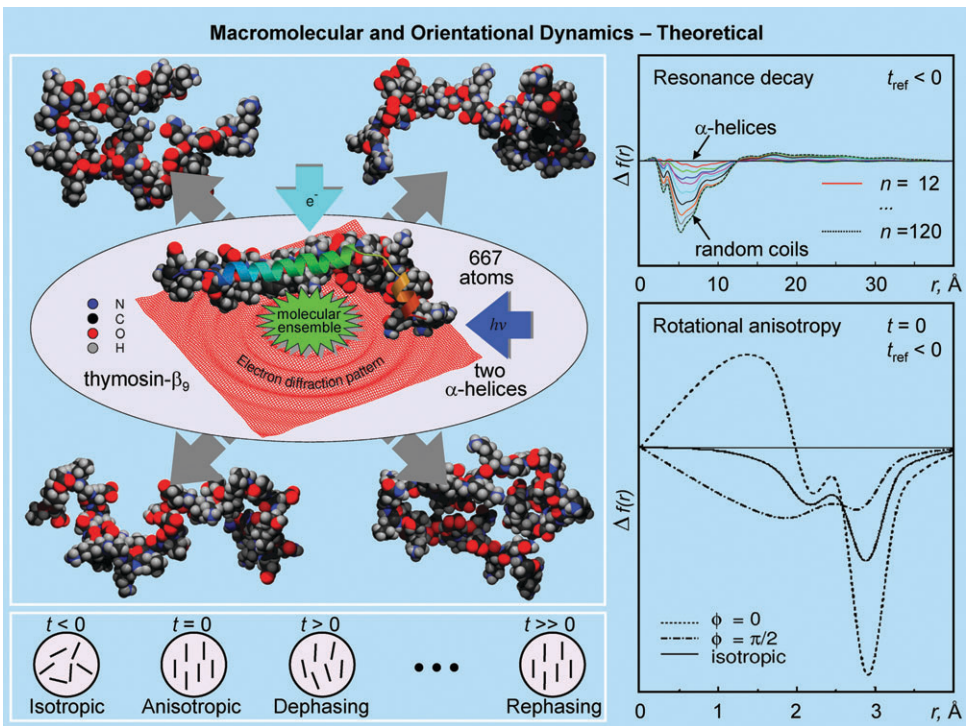

Fig. 11 Macromolecular ensembles and orientation in diffraction. Theoretical UED studies of the helix-to-coil transition for an ensemble of thymosin-β_9; the schematic representation in the middle inset (upper left) is to indicate a laser-induced temperature jump. Ensemble-averaged diffraction differences obtained for 2^{10} partially-randomized α-helical molecular structures were calculated with respect to the reference experimentally determined structure of the protein, which is characteristic of negative times. The number of arbitrarily altered dihedral angles in the backbone chain of the protein, n, increases monotonically from the center to the bottom of the panel (upper right). Evolving ensemble orientation in the interaction volume is depicted as a function of time (lower left). Slices of anisotropic diffraction difference patterns of the dissociation of CF_3I with a reference to negative times as obtained for $\phi = 0$ and $\phi = \pi/2$, and $\delta = \pi/2$, immediately after passage of the laser light ($t = 0$) are shown, see ref. 37 for details. Also plotted are the patterns that would apply if the same populations were distributed isotropically (lower right).

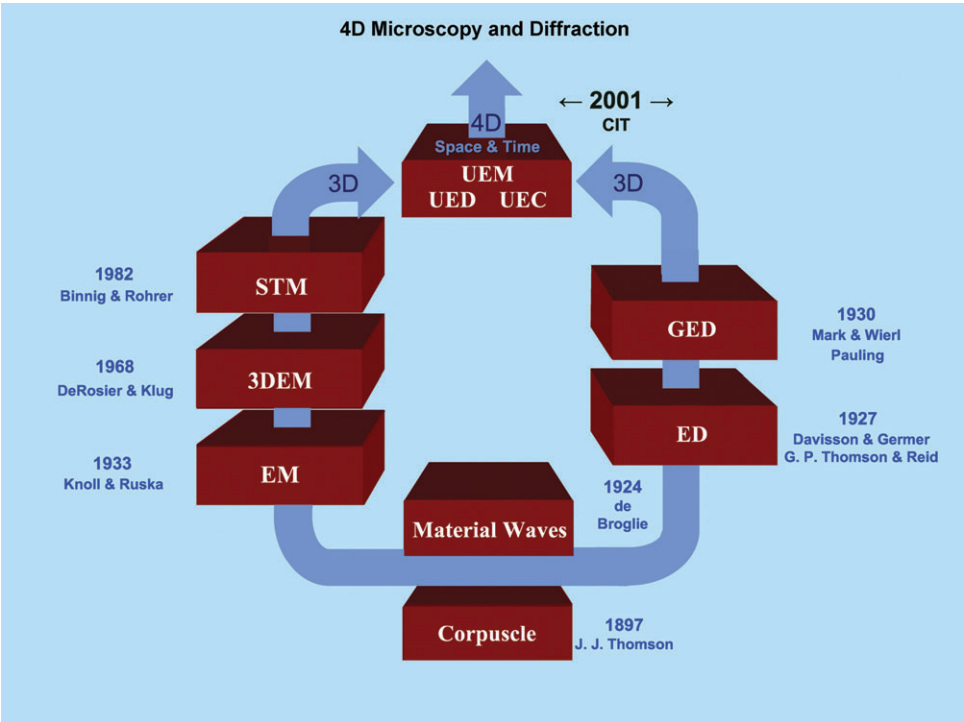

Fig. 12 A brief history of developments in 3D and 4D imaging, microscopy and diffraction, displaying milestones, since the discovery of the electron (corpuscle) in 1897, for reaching the atomic-scale spatial (3D) and spatiotemporal (4D) resolutions. With these advances, fields of study have opened up in a variety of disciplines,[4] and elsewhere the contributions by colleagues in these developments have been summarized.[3,9]

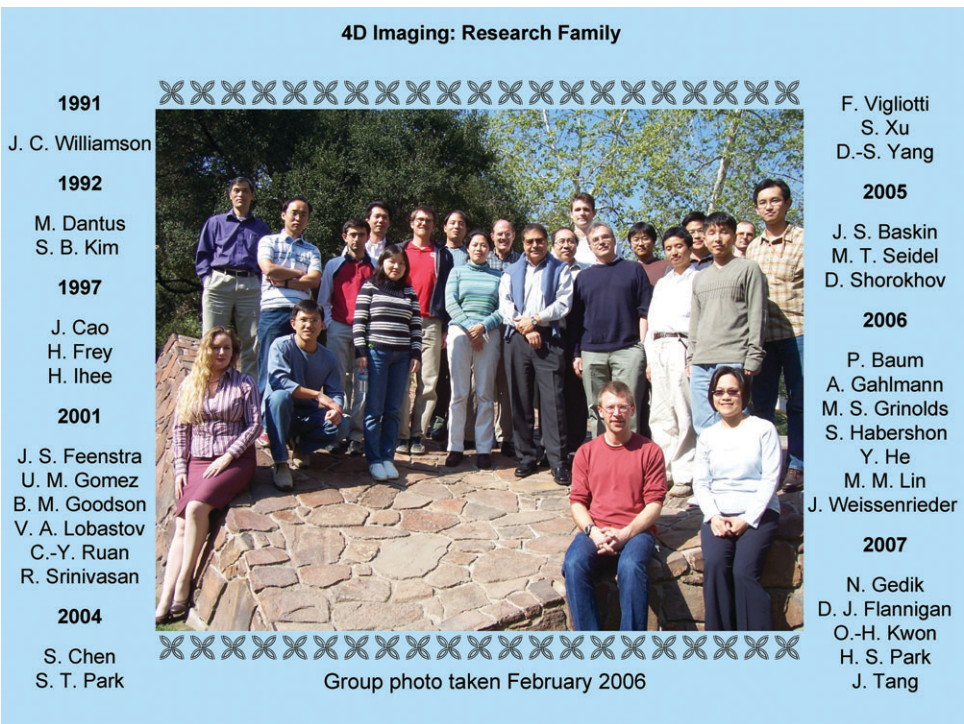

Fig. 13 The research family. Major contributors in imaging research are listed in chronological order defined by the year when the account of their pertinent research first appeared in press. The contributors are listed alphabetically within a year (see Acknowledgements).

in this regard. Recently, a systematic theoretical study of nonequilibrium structural dynamics for a quasi-1D substrate–adsorbate lattice was carried out and compared with experimental results of UEC. Using a lattice model of a chain of atoms, including anharmonic forces (Fig. 8), we investigated influences of the impulsive force on the temporal behavior of Bragg diffraction. The roles of force-constant mismatch, frictional damping and substrate-to-adsorbate coupling were also examined in detail.[28] The results elucidated the importance of coherent wave propagation in the nonequilibrium regime and provided the atomic-scale description of both surface and bulk dynamics. The observed large-amplitude expansion results from a coherent, nonlocal sound-wave effect. This conclusion is fundamentally significant in that the observed lattice expansion deduced from the Bragg spot movement is not necessarily linked to conventional thermal expansions due to a temperature rise.[28]

At longer times, a common feature in the UEM and UEC studies of materials is the spatial diffusion of energy (and carriers) in 2D or 3D, depending on the structure. Given the nature of the experimental impulse used, it is straightforward to model such diffusion processes, and comparison with the experimental results can be made directly.[40] However, when nm-scale crystallites undergo a change, such as a phase transition, one has to consider the time scale of connectivity in the material and the density of carriers involved. Such considerations have theoretically been expressed and account for the general UEM transient behavior.[20] What remains to be addressed is the meaning of phase transitions and recovery on the nm-length scale.

Given the progress made in quantum chemistry methods, both molecular and electronic structures of many compounds can now be pictured in a matter of hours of computation time on a high-end PC. As it is the electron density distribution in real space $\rho(\boldsymbol{r})$, $\boldsymbol{r} = (x, y, z)$, which determines both the spatial structure and the chemical reactivity of a molecule, calculated frames of $\rho(\boldsymbol{r})$ provide a quantitative insight into the dynamics of chemical bonding across the molecular framework. Theoretical atoms-in-molecules (AIM) studies of heteroaromatic compounds recently carried out in this laboratory provided a possible rationalization for the lack, or near-absence, of the nonradiative decay channel characteristic of lutidine, as opposed to pyridine or picoline.[41] A topological comparison of ground-state and lowest-lying excited-state electronic structures of these molecules reveals that bifurcations into radiative and radiationless decay processes may be associated with competing electron excitation mechanisms. Similarly, topological analyses of the total electron densities characteristic of the ground-state and electronically excited-state structures of benzaldehyde were used to account for diffraction differences between the electronic ground state (S_0), the lowest-lying $n\pi^*$ excited states (S_1, T_1), and the lowest-lying $\pi\pi^*$ excited state (T_2; *quinoid*) of the molecule. Applicability of AIM analysis to the quantification of the strength of a hydrogen bond was illustrated as well.[33]

With our newly-designed supercomputer cluster which currently features 32 dual-quad-core E5345 Intel Xeon compute nodes, 12 GB RAM/node, 10 TB of disk storage space and a gigabit ethernet interconnection mesh, we are poised to explore ultrafast nonequilibrium dynamics of complex energy landscapes pertinent to physical, chemical or biological processes. Structure interconversions which involve multiple degrees of freedom, such as conformational changes in biological macromolecules, can now be modeled, and the ensemble convergence can be achieved at increasingly longer time scales. An example of such capability comes from our studies of the energy landscape of a protein. An invariant description of the landscape is incomplete because fluctuations in volume, and thus in pressure, are inevitably present on the molecular length scale. To examine the impact of microscopic statistical pressure fluctuations on both the topology and the dissipation characteristics of the landscape, ns MD simulations of hen-egg-white lysozyme were recently carried out in this laboratory.[42]

Another area of focus is that of the experimental and theoretical studies of folding–unfolding dynamics. Even for a small macromolecule, such as a DNA hairpin, the complexity of the energy landscape demands these new tools of computations. Stimulated by recent observations of denatured intermediate states for a 5′-CCCCTT-X_{13}-AAGGGG-3′ DNA hairpin at temperatures higher than the melting temperature, as evidenced by absorption/fluorescence-quenching experiments,[43] we performed ensemble-convergent MD simulations on a similar, benchmark 5′-ATCCTA-X_4-TAGGAT-3′ DNA hairpin. But, concurrently, we developed a simple analytical model of DNA unzipping based on tabulated pairing–stacking thermodynamic parameters and loop entropy. Specifically, the model elucidates the dependence of the unzipping behaviour on the stem sequence and length of the loop. After verifying the assumptions and predictions of the model *via* MD simulations on the benchmark hairpin, we invoked the stem-sequence and loop-length permutations of the 5′-CCCCTT-X_{13}-AAGGGG-3′ hairpin to study the entropic and enthalpic factors that determine hairpin stability. For a wide range of such permutations of the hairpin, it was important to determine the temperature range for which the two-state hypothesis breaks down as well as the base-pairing configuration of the intermediate state.[44]

5. Conclusion and outlook

The progress made in electron imaging over a century of development is truly remarkable. From the milestones highlighted in Fig. 12, the origins of the two branches (3D microscopy and diffraction) stem from J. J. Thomson's discovery of the electron and L. de Broglie's concept of particle–wave duality, as mentioned above. Up to the beginning of this century, the development was mainly limited to 2D and 3D static structures, but only over the past decade did ultrafast 4D electron imaging in space and time become possible. Elsewhere, more details are given of the historical evolutions and revolutions,[3,9] and for a highlight perspective the reader is referred to the commentaries and comprehensive review by J. M. Thomas.[4] What is clear from the diverse applications discussed here is that the methodology has the potential for applications in many disciplines of physics, chemistry and biology. Naturally, the study of chemical reactions, interfaces and phase transitions will continue both experimentally and theoretically. And, perhaps, the *in situ* observations of

phenomena of nm-length scale may constitute a major area of study in materials science, using single-electron and single-pulse UEM. Just as electron microscopy has become a standard tool for static imaging for over fifty years, adding the fourth dimension—with real-space (atomic-scale), energy-space and Fourier-space capabilities—should have a similar impact on the determination of structural dynamics, including those of biological systems.

Acknowledgements†

This research was supported by the National Science Foundation, the Air Force Office of Scientific Research and the Gordon and Betty Moore Foundation. We would like to express our sincere gratitude to members of our laboratories, past and present (see Fig. 13), who contributed significantly to the research discussed here in UED, UEC and UEM.

References

1 A. H. Zewail, *Angew. Chem., Int. Ed.*, 2000, **39**, 2587–2631originally published in: *Les Prix Nobel: The Nobel Prizes 1999*, ed. T. Frängsmyr, Almqvist & Wiksell, Stockholm, 2000, pp. 110–203, and references therein.
2 J. C. Polanyi and A. H. Zewail, *Acc. Chem. Res.*, 1995, **28**, 119–132.
3 A. H. Zewail, *Annu. Rev. Phys. Chem.*, 2006, **57**, 65–103, and references therein.
4 J. M. Thomas, in *Physical Biology: From Atoms to Medicine*, ed. A. H. Zewail, Imperial College Press, London, 2008, pp. 51–113; J. M. Thomas, *Angew. Chem., Int. Ed.*, 2005, **44**, 5563–5566; K. D. M. Harris and J. M. Thomas, *Cryst. Growth Des.*, 2005, **5**, 2124–2130; J. M. Thomas, *Angew. Chem., Int. Ed.*, 2004, **43**, 2606–2610; J. M. Thomas, *Nature*, 1991, **351**, 694–695.
5 C. Bressler and M. Chergui, *Chem. Rev.*, 2004, **104**, 1781–1812, and references therein.
6 L. R. Maxwell, *Phys. Rev.*, 1933, **44**, 73–76; S. Lengyel and E. Kalman, *Nature*, 1974, **248**, 405–406.
7 J. S. Baskin and A. H. Zewail, *J. Chem. Educ.*, 2001, **78**, 737–751.
8 A. H. Zewail, *Nature*, 2001, **412**, 279; A. H. Zewail, *Angew. Chem., Int. Ed.*, 2001, **40**, 4371–4375.
9 A. H. Zewail, in *Visions of Discovery: New Light on Physics, Cosmology and Consciousness*, Cambridge University Press, Cambridge, 2008, in press.
10 P. Baum and A. H. Zewail, *Proc. Natl. Acad. Sci. U. S. A.*, 2007, **104**, 18409–18414.
11 A. H. Zewail and V. A. Lobastov, *US Pat.*, 7 154 091, 2006.
12 H. S. Park, J. S. Baskin, O.-H. Kwon and A. H. Zewail, *Nano Lett.*, 2007, **7**, 2545–2551.
13 H. Ihee, V. A. Lobastov, U. M. Gomez, B. M. Goodson, R. Srinivasan, C.-Y. Ruan and A. H. Zewail, *Science*, 2001, **291**, 458–462; H. Ihee, B. M. Goodson, R. Srinivasan, V. A. Lobastov and A. H. Zewail, *J. Phys. Chem. A*, 2002, **106**, 4087–4103.
14 D. Zhong, S. Ahmad and A. H. Zewail, *J. Am. Chem. Soc.*, 1997, **119**, 5978–5979.
15 H. Ihee, J. Kua, W. A. Goddard III and A. H. Zewail, *J. Phys. Chem. A*, 2001, **105**, 3623–3632.
16 C.-Y. Ruan, V. A. Lobastov, F. Vigliotti, S. Chen and A. H. Zewail, *Science*, 2004, **304**, 80–84.
17 S. K. Pal and A. H. Zewail, *Chem. Rev.*, 2004, **104**, 2099–2123; W. Qiu, Y.-T. Kao, L. Zhang, Y. Yang, L. Wang, W. E. Stites, D. Zhong and A. H. Zewail, *Proc. Natl. Acad. Sci. U. S. A.*, 2006, **103**, 13979–13984.
18 P. P. Edwards, R. L. Johnston, C. N. R. Rao, D. P. Tunstall and F. Hensel, *Philos. Trans. R. Soc. London, Ser. A*, 1998, **356**, 5–22, and references therein.
19 M. S. Grinolds, V. A. Lobastov, J. Weissenrieder and A. H. Zewail, *Proc. Natl. Acad. Sci. U. S. A.*, 2006, **103**, 18427–18431.
20 V. A. Lobastov, J. Weissenrieder, J. Tang and A. H. Zewail, *Nano Lett.*, 2007, **7**, 2552–2558.
21 P. Baum, D.-S. Yang and A. H. Zewail, *Science*, 2007, **318**, 788–792.
22 The ps structural transformation projects along the *c* and *b* axes. If the fs motion had large components along *b* or *c*, it would show up in the dynamics of all investigated spots, contrary to observations.
23 N. Gedik, D.-S. Yang, G. Logvenov, I. Bozovic and A. H. Zewail, *Science*, 2007, **316**, 425–429.
24 The error range in the determination of the absolute values of the lattice constants comes from the uncertainty in determining the sample-to-camera distance. However, relative changes can be measured with much better accuracy, reaching below 0.01 Å.
25 F. Carbone, P. Baum, P. Rudolf and A. H. Zewail, *Phys. Rev. Lett.*, 2008, **100**, 035501.
26 M. T. Seidel, S. Chen and A. H. Zewail, *J. Phys. Chem. C*, 2007, **111**, 4920–4938; S. Chen, M. T. Seidel and A. H. Zewail, *Proc. Natl. Acad. Sci. U. S. A.*, 2005, **102**, 8854–8859.
27 S. Chen, M. T. Seidel and A. H. Zewail, *Angew. Chem., Int. Ed.*, 2006, **45**, 5154–5158.
28 J. Tang, D.-S. Yang and A. H. Zewail, *J. Phys. Chem. C*, 2007, **111**, 8957–8970.
29 C.-Y. Ruan, D.-S. Yang and A. H. Zewail, *J. Am. Chem. Soc.*, 2004, **126**, 12797–12799.
30 V. A. Lobastov, R. Srinivasan and A. H. Zewail, *Proc. Natl. Acad. Sci. U. S. A.*, 2005, **102**, 7069–7073.
31 D. J. Flannigan, V. A. Lobastov and A. H. Zewail, *Angew. Chem., Int. Ed.*, 2007, **46**, 9206–9210.
32 P. Baum and A. H. Zewail, *Proc. Natl. Acad. Sci. U. S. A.*, 2006, **103**, 16105–16110.
33 D. Shorokhov, S. T. Park and A. H. Zewail, *ChemPhysChem*, 2005, **6**, 2228–2250, and references therein.
34 K. D. M. Harris, S. Habershon, E. Y. Cheung and R. L. Johnston, *Z. Kristallogr.*, 2004, **219**, 838–846.
35 S. Habershon and A. H. Zewail, *ChemPhysChem*, 2006, **7**, 353–362.
36 M. M. Lin, D. Shorokhov and A. H. Zewail, *Chem. Phys. Lett.*, 2006, **420**, 1–7.
37 J. S. Baskin and A. H. Zewail, *ChemPhysChem*, 2005, **6**, 2261–2276; J. S. Baskin and A. H. Zewail, *ChemPhysChem*, 2006, **7**, 1562–1574.
38 J. C. Williamson and A. H. Zewail, *J. Phys. Chem.*, 1994, **98**, 2766–2781.
39 C.-Y. Ruan, V. A. Lobastov, R. Srinivasan, B. M. Goodson, H. Ihee and A. H. Zewail, *Proc. Natl. Acad. Sci. U. S. A.*, 2001, **98**, 7117–7122.
40 D.-S. Yang, N. Gedik and A. H. Zewail, *J. Phys. Chem. C*, 2007, **111**, 4889–4919.
41 R. Srinivasan, J. S. Feenstra, S. T. Park, S. Xu and A. H. Zewail, *Science*, 2005, **307**, 558–563.
42 L. Meinhold, J. C. Smith, A. Kitao and A. H. Zewail, *Proc. Natl. Acad. Sci. U. S. A.*, 2007, **104**, 17261–17265.
43 H. Ma, C. Wan, A. Wu and A. H. Zewail, *Proc. Natl. Acad. Sci. U. S. A.*, 2007, **104**, 712–716.
44 M. M. Lin, L. Meinhold, D. Shorokhov and A. H. Zewail, *Phys. Chem. Chem. Phys.*, 2008, submitted.
45 Y. He, A. Gahlmann, J. S. Feenstra, S. T. Park and A. H. Zewail, *Chem.–Asian J.*, 2006, **1–2**, 56–63.
46 S. T. Park, J. S. Feenstra and A. H. Zewail, *J. Chem. Phys.*, 2006, **124**, 174707.
47 J. S. Feenstra, S. T. Park and A. H. Zewail, *J. Chem. Phys.*, 2005, **123**, 221104.
48 S. Xu, S. T. Park, J. S. Feenstra, R. Srinivasan and A. H. Zewail, *J. Phys. Chem. A*, 2004, **108**, 6650–6655.
49 F. Vigliotti, S. Chen, C.-Y. Ruan, V. A. Lobastov and A. H. Zewail, *Angew. Chem., Int. Ed.*, 2004, **43**, 2705–2709.
50 R. Srinivasan, J. S. Feenstra, S. T. Park, S. Xu and A. H. Zewail, *J. Am. Chem. Soc.*, 2004, **126**, 2266–2267.
51 C.-Y. Ruan, F. Vigliotti, V. A. Lobastov, S. Chen and A. H. Zewail, *Proc. Natl. Acad. Sci. U. S. A.*, 2004, **101**, 1123–1128.
52 B. M. Goodson, C.-Y. Ruan, V. A. Lobastov, R. Srinivasan and A. H. Zewail, *Chem. Phys. Lett.*, 2003, **374**, 417–424.

† In this perspective, the contributions made by the Caltech group are indicated in ref. 10–13, 15, 16, 19–21, 23, 25–33, 35–41 and 45–64.

53 H. Ihee, J. S. Feenstra, J. Cao and A. H. Zewail, *Chem. Phys. Lett*., 2002, **353**, 325–334.
54 V. A. Lobostov, R. Srinivasan, B. M. Goodson, C.-Y. Ruan, J. S. Feenstra and A. H. Zewail, *J. Phys. Chem. A*, 2001, **105**, 11159–11164.
55 H. Ihee, J. Cao and A. H. Zewail, *Angew. Chem., Int. Ed*., 2001, **40**, 1532–1536.
56 H. Ihee, A. H. Zewail and W. A. Goddard III, *J. Phys. Chem. A*, 1999, **103**, 6638–6649.
57 J. Cao, H. Ihee and A. H. Zewail, *Proc. Natl. Acad. Sci. U. S. A*., 1999, **96**, 338–342.
58 J. Cao, H. Ihee and A. H. Zewail, *Chem. Phys. Lett*., 1998, **290**, 1–8.
59 H. Ihee, J. Cao and A. H. Zewail, *Chem. Phys. Lett*., 1997, **281**, 10–19.
60 J. C. Williamson, J. Cao, H. Ihee, H. Frey and A. H. Zewail, *Nature*, 1997, **386**, 159–162.
61 M. Dantus, S. B. Kim, J. C. Williamson and A. H. Zewail, *J. Phys. Chem*., 1994, **98**, 2782–2796.
62 J. C. Williamson and A. H. Zewail, *Chem. Phys. Lett*., 1993, **209**, 10–16.
63 J. C. Williamson, M. Dantus, S. B. Kim and A. H. Zewail, *Chem. Phys. Lett*., 1992, **196**, 529–534.
64 J. C. Williamson and A. H. Zewail, *Proc. Natl. Acad. Sci. U. S. A*., 1991, **88**, 5021–5025.